



Improving typhoon predictions by assimilating the retrieval of atmospheric temperature profiles from the FengYun-4A's Geostationary Interferometric Infrared Sounder (GIIRS)

Jie Feng^{a,b}, Xiaohao Qin^{b,*}, Chunqiang Wu^{c,d}, Peng Zhang^e, Lei Yang^e, Xueshun Shen^d, Wei Han^d, Yongzhu Liu^d

^a Department of Atmospheric and Oceanic Sciences and Institute of Atmospheric Sciences, Fudan University, Shanghai, China

^b State Key Laboratory of Numerical Modeling for Atmospheric Sciences and Geophysical Fluid Dynamics (LASG), Institute of Atmospheric Physics, Chinese Academy of Sciences, Beijing, China

^c Key Laboratory of Radiometric Calibration and Validation for Environmental Satellites, National Satellite Meteorological Center, China Meteorological Administration, Beijing, China

^d CMA Earth System Modeling and Prediction Centre (CEMC), China Meteorological Administration, Beijing, China

^e Innovation Center for FengYun Meteorological Satellite, National Satellite Meteorological Center, China Meteorological Administration, Beijing, China

ARTICLE INFO

Keywords:
Typhoons
Targeting observations
CNOP
FY-4A satellite
Infrared sounder
Data assimilation

ABSTRACT

The Geostationary Interferometric Infrared Sounder (GIIRS) onboard China's FengYun-4A geostationary satellite provides an unprecedented opportunity to observe the three-dimensional thermodynamic structure of typhoons in the western North Pacific Ocean with high spatiotemporal resolutions. Field campaigns of targeting observation based on the conditional nonlinear optimal perturbation (CNOP) sensitivity were carried out utilizing the GIIRS on FY-4A for five typhoons: Chan-hom, Maysak, and Higos in 2020 and typhoons Chanthu and Conson in 2021 and collected temporally continuous observations for the thermodynamic structure of typhoons and their environments.

This study investigated the impact of atmospheric temperature profile retrieved from the collected GIIRS radiance on typhoon analysis and prediction in a regional Hurricane WRF (HWRF) model using the ensemble-variational data assimilation scheme. Despite the case dependence, the assimilation of the additional satellite retrieval generally improves the typhoon track forecasts relative to those with simply the operational observations assimilated. The improvement mainly occurs beyond two days and the average reduction of track errors reaches up to 100 km at about day 3. Diagnostics show that the improvement of initial temperature condition influences the geopotential height and wind fields roughly through the hydrostatic relationship. The assimilation of temperature retrieval also shows some potential in improving wind forecasts in the near-coast areas at upper and lower levels and the precipitation forecasts on land.

1. Introduction

Despite a significant improvement in the prediction skill of tropical cyclones (TCs) in the last few decades, there are still challenges in predicting the track and landfall of some TCs, especially those with complex paths influenced by multiple interactive synoptic systems (e.g., Wu et al., 2004; Torn et al., 2015; Nystrom et al., 2018). Novel observing systems for monitoring and observing TCs and the surrounding environment are important in data assimilation (DA) and numerical forecasts of TCs (Weng and Zhang, 2012; Wu et al., 2014; Minamide and

Zhang, 2018; Lu and Wang, 2020).

Meteorological satellites provide a useful supplementary platform for the temporal and spatial sampling of geophysical systems, especially over the oceans where conventional observations are sparse. The main satellite-based measurements are direct radiance or brightness temperature observations from sounders onboard meteorological satellites, such as microwave and infrared sounders (Li and Liu, 2009). In particular, the infrared sounders have hundreds of channels that can provide detailed atmospheric profiles of temperature and humidity with high vertical resolution (Wang et al., 2007). However, most existing sounder

* Corresponding author.

E-mail address: xhjin@lasg.iap.ac.cn (X. Qin).

instruments are all onboard polar-orbiting satellites (Chahine et al., 2006; Clerbaux et al., 2007; Smith sr et al., 2009; Bloom, 2001).

After nearly 30 years of development, Chinese meteorological satellites, typified by the Fengyun series, have achieved outstanding progress. The latest generation of the Fengyun geostationary meteorological satellite (FY-4A) was successfully launched in 2016 (Yang et al., 2017; Menzel et al., 2018). FY-4A is the first geostationary weather satellite to carry the Geostationary Interferometric Infrared Sounder (GIIRS; Yang et al., 2017; Di et al., 2018; Schmetz, 2021). The GIIRS has hundreds of long- and mid-wave channels which facilitates the ability to continuously sample temperature and humidity profiles of the atmosphere with high vertical resolution in targeted regions (Yang et al., 2017).

Progress has been made in improving the bias correction and quality control algorithms (e.g., Yin et al., 2020) and developing efficient retrieval models (e.g., Di et al., 2018; Ma et al., 2021) for GIIRS radiance observations, which greatly promoted the application of GIIRS data in global and regional numerical weather prediction (NWP) models. Radiance measurements from the FY-4A GIIRS have been directly assimilated into the global 4D-Var assimilation system of the China Meteorological Administration (CMA) operational Global/Regional Assimilation and PrEdiction System (GRAPES) since 2018. Yin et al. (2021) investigated the impact of the direct assimilation of GIIRS radiance in the operational system configurations on the prediction of a single typhoon (referred to as TCs in the northwest Pacific) Maria (2018). They concluded that the direct assimilation of the GIIRS radiance with high temporal resolution had a positive contribution to the forecast of typhoon tracks. Nevertheless, more cases are needed to evaluate the impacts of assimilating GIIRS data on TC analyses and forecasts, and the mechanisms of such impacts need to be examined, which are not addressed in Yin et al. (2021). In addition, the assimilation of the vertical temperature and moisture profile retrieved from the GIIRS radiance observations has not been studied yet, which could offer a further evaluation of the effects of GIIRS observations on TC forecasts.

Due to the spatiotemporal continuity and mobility of observations, the CMA, in cooperation with the Institute of Atmospheric Physics and Fudan University in China, utilized the FY-4A GIIRS to conduct a series of field campaigns of targeting observation for typhoons in the western North Pacific Ocean in the 2020 and 2021 (see Section 2.1). These field campaigns provide unprecedented opportunities to comprehensively investigate the impact of the FY-4A GIIRS retrievals on the analysis and prediction of multiple targeted typhoons. All these will be addressed in this study using an advanced data assimilation (DA) scheme [the ensemble variational (EnVar) method] based on a high-resolution regional model—the Hurricane Weather Research and Forecasting (HWRF) model. This paper is organized as follows. Section 2 describes the basic information about the GIIRS retrieval observations and the preprocess of retrieval data for assimilation. Section 3 introduces the configuration of the forecast model, the DA scheme, and the experimental design. The impact of assimilating the GIIRS retrieval on TC track predictions and its relevant mechanisms are detailed in Section 4. Section 5 evaluates the assimilation impact on predictions of wind and rainfall. Section 6 gives the conclusions and discussion.

2. Atmospheric profile retrieval of GIIRS and preprocess

2.1. Targeting observations with FY-4A GIIRS

The GIIRS onboard the FY-4A satellite can monitor the atmospheric and surface temperature and humidity at a high time frequency of 15 min. Under the current operational observing mode, FY-4A GIIRS samples the region over China every 120 min with a nominal nadir resolution of 16 km. The instrument has 1650 channels in two separate infrared spectral regions: 689 channels in the longwave infrared band ($700\text{--}1130\text{ cm}^{-1}$) and 961 channels in the shortwave infrared band ($1650\text{--}2250\text{ cm}^{-1}$). Such a high spectral resolution can resolve the

atmospheric vertical profile to 101 vertical levels. More information about FY-4A/GIIRS can be referred to Yang et al. (2017), Zhang et al. (2019), and Xian et al. (2021). The atmospheric and surface thermodynamic variables are retrieved using the FY-4A/GIIRS observed radiance (converted to the brightness temperature) under both clear and cloudy conditions. Both the statistical regression retrieval algorithm and the nonlinear physical retrieval algorithm developed by Li et al. (2000) are implemented under clear sky conditions. Under cloudy conditions, the atmospheric variables are retrieved based on the physical dual-regression method introduced by Smith Sr. et al. (2012).

In virtue of the advantages of the GIIRS onboard the geostationary FY-4A satellite, it was used to implement the field campaigns of targeting observations for five typhoons, i.e., Chan-hom, Maysak, and Higos in 2020 and typhoons Chanthu and Conson in 2021,. Table 1 gives the lifetimes of these typhoons with the intensity of a tropical storm and above ($\geq 17.2\text{ m s}^{-1}$). In the determining stage, the sensitive regions, i.e., where the initial errors of numerical models will probably induce the largest forecast errors, were identified by the conditional nonlinear optimal perturbation method (CNOP; Mu et al., 2003, 2009). That is, eliminating the initial errors that the CNOP sensitivity indicates will greatly improve the subsequent TC forecasts (Qin and Mu, 2011; Qin et al., 2022). Then, the operational scanning path of the GIIRS was adaptively adjusted to observe the aforementioned sensitive regions and their surroundings.

2.2. Preprocess of retrieval observations

We assimilated the satellite retrieval of the vertical temperature profile with a quality flag of 0 (“very good”). Fig. 1 shows the specified error standard deviations of the temperature profile retrieval at different levels. The standard deviation of the observational errors is 2.0 K above 600 hPa and then linearly increases to 4.0 K downward to the sea surface, which is approximately optimal in our preliminary experimental evaluation.

Although only observations with high standard quality control (quality flag 0) were selected, their spatiotemporal resolution was still high, which may not be optimal for the model configuration of our DA system. We therefore further thinned the observations using the super-obbing strategy to better match the model resolution (Alpert and Kumar, 2007; Feng and Wang, 2019, 2021). Specifically, observations within a defined spatial prism ($\Delta x \times \Delta y \times \Delta z$) and temporal interval Δt were averaged and their position and time information were used to construct a single observation. Δx and Δy were 0.3° (about 30 km), roughly five times the model grid size (6 km; see Section 3.1), and Δz spanned almost two model layers. Our preliminary evaluation showed limited sensitivity of the TC track forecasts to the selection of Δx and Δy around 30 km (not shown). Δt was 30 min, approaching an optimum performance as concluded in Yin et al. (2021).

3. Systems and experiments

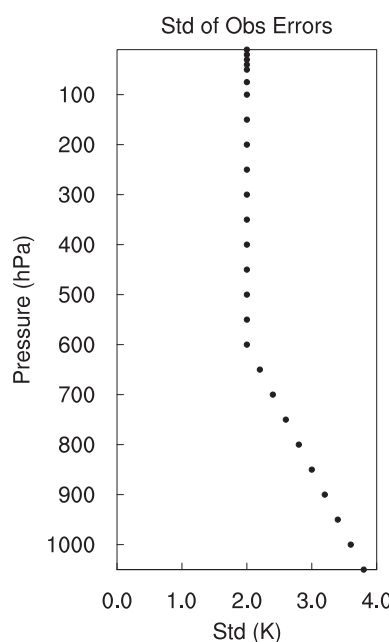
3.1. HWRF model configuration

We use the HWRF model version 3.9a in this study, which is the 2017 operational model for hurricane prediction implemented at National Centers for Environmental Prediction (NCEP; Biswas et al., 2017). The operational model configuration has three nested domains with 18/6/2-km ($0.135^\circ/0.045^\circ/0.015^\circ$) horizontal resolution and 61 vertical levels with a model top at 2 hPa (Biswas et al., 2017). Different from the operational configuration, the HWRF model in our experiments adopts only the outer two nested domains (i.e., the 18- and 6-km grid spacing). The outer (D01) and inner (D02) domains contain 288×576 and 304×604 horizontal grid points (approximately $80^\circ \times 80^\circ$ and $27^\circ \times 27^\circ$ in size, respectively). The inner domain has movable two-way interactive nest grids that follow the projected path of a TC. The HWRF model physics in this study uses the default setup of HWRF v3.9a which is

Table 1

Basic information about studied typhoons.

Typhoon	Case No.	Duration	Maximum intensity and time	Analysis time	Forecast length (days)	Period of precipitation verification
Chanthom	1	0000 UTC 5 Oct–1200 UTC 11 Oct, 2020	38 m s ⁻¹ , 965 hPa, 0000 UTC 09 Oct	0600 UTC 8 Oct, 2020	3	30–54 h
	2			1800 UTC 8 Oct, 2020	3	18–42 h
Maysak	3	1200 UTC 28 Aug–0000 UTC 4 Sep, 2020	52 m s ⁻¹ , 940 hPa, 0600 UTC 01 Sep	0600 UTC 31 Aug, 2020	3	54–72 h
	4			1800 UTC 31 Aug, 2020	3	42–66 h
Higos	5	0000 UTC 18 Aug–0600 UTC 19 Aug, 2020	35 m s ⁻¹ , 970 hPa, 1800 UTC 18 Aug	0600 UTC 18 Aug, 2020	1.25	6–30 h
Chanthu	6	0000 UTC 7 Sep–1800 UTC 17 Sep, 2021	68 m s ⁻¹ , 905 hPa, 1200 UTC 10 Sep	1800 UTC 8 Sep, 2021	4	66–90 h
	7			0600 UTC 9 Sep, 2021	4	54–78 h
Conson	8	0600 UTC 6 Sep–0000 UTC 12 Sep, 2021	30 m s ⁻¹ , 982 hPa, 0600 UTC 08 Sep	1800 UTC 8 Sep, 2021	3.5	66–84 h

**Fig. 1.** Standard deviation (Std) of the observational errors of the FY-4A GIIRS vertical temperature profile retrieval.

summarized in Table 2 (see more details in Biswas et al., 2017).

3.2. Data assimilation system

The DA experiments are performed using the GSI-based EnVar assimilation for HWRF (Lu et al., 2017a, 2017b), extended from the GSI EnVar DA for the global prediction system (Wang et al., 2013). As pointed out in Section 3.1, HWRF is configured with two nested domains (i.e., D01 and D02) on the 18- and 6-km grids, and the DA step is implemented simply for D02. We do not run cycling DA experiments because, in our data archive, the operational Global Ensemble Forecast System (GEFS) products at NCEP are only available at 0000Z and 1200Z each day. For each case, the initial conditions for running the HWRF background control and ensemble forecasts are interpolated directly from the global analysis of the operational Global Forecast System (GFS) and the global ensemble analyses of the operational GEFS at NCEP, respectively (i.e., cold start initialization). The background (or first guess) fields for D02 use the 3-hourly control forecasts of HWRF valid at 3, 6, and 9 h initialized from the downscaled GFS analysis to better match the observation time within the DA window. The ensemble-based error covariance for D02 is calculated from 20 6-hourly HWRF ensemble forecasts from the downscaled ensemble analyses from the GEFS. The control analysis is updated using the EnVar scheme in GSI. More details about the EnVar algorithm can be referred to Wang (2010).

In our experiments, for the DA in the 6-km domain (D02), the full ensemble covariance without combining the static covariance is used as suggested by Lu et al. (2017b) and Feng and Wang (2019). They found

Table 2

Description of the experimental setup.

Experiments	Model resolution	Inner domain (D02)	Parent domain (D01)	Model physics	Observations assimilated
BASE	18/6 km and 61 levels;	Gridpoint Statistical Interpolation (GSI)-based, ensemble-variational (En-Var) data assimilation system for Hurricane Weather Research and Forecasting (HWRF) Model	Global Forecast System (GFS)	Simplified Arakawa-Schubert (SAS) cumulus parameterization scheme, and the Ferrier-Aligo microphysics scheme; GFS Hybrid-EDMF planetary boundary layer scheme; HWRF surface layer scheme and Noah Land Surface Model; the RRTMG longwave and shortwave radiation schemes.	Operational observations (conventional observations in prepbufr; satellite radiances from AMSU-A, and ATMS; GPS radio occultation and bending angle observations)
BASE+ GIIRS					All obs in BASE and vertical temperature profile retrieval from GIIRS on FY-4A

that combining the static background error covariance degraded the performance of DA and prediction for TCs in a similar HWRF and DA system framework. The ensemble covariance is spatially localized with a horizontal e-folding distance of 180 km and a vertical e-folding width of nearly 150 hPa following our previous studies on TC assimilation (Feng and Wang, 2019, 2021).

3.3. Experimental design

All the available observations within the 6-hour time window centered at the analysis time are assimilated in the D02 domain (6-km grid spacing). To evaluate the impact of assimilating the GIIRS retrieval data on TC analysis and prediction, we designed two experiments for

each Typhoon case for comparison. In the baseline experiment (“BASE”), the observations ingested in the operational global DA system of CMA are assimilated into the GSI-based regional HWRF system, including conventional observations, AMSU-A and ATMS radiance observations, and GPS radio occultation and bending angle observations (see more details in Table 2). The other experiment (named “BASE+GIIRS”) assimilates the superobbed vertical temperature profile data from FY-4A GIIRS in addition to all the observations in BASE.

Once deriving the initial analysis of D02, the free forecasts are produced on the 18/6-km grids with an output frequency of 6 h. The forecast lead times are different for individual typhoons (see Table 1) due to their different lifetimes. The best-track data for the verification of TC track forecasts are from the CMA Tropical Cyclone Data Center. The

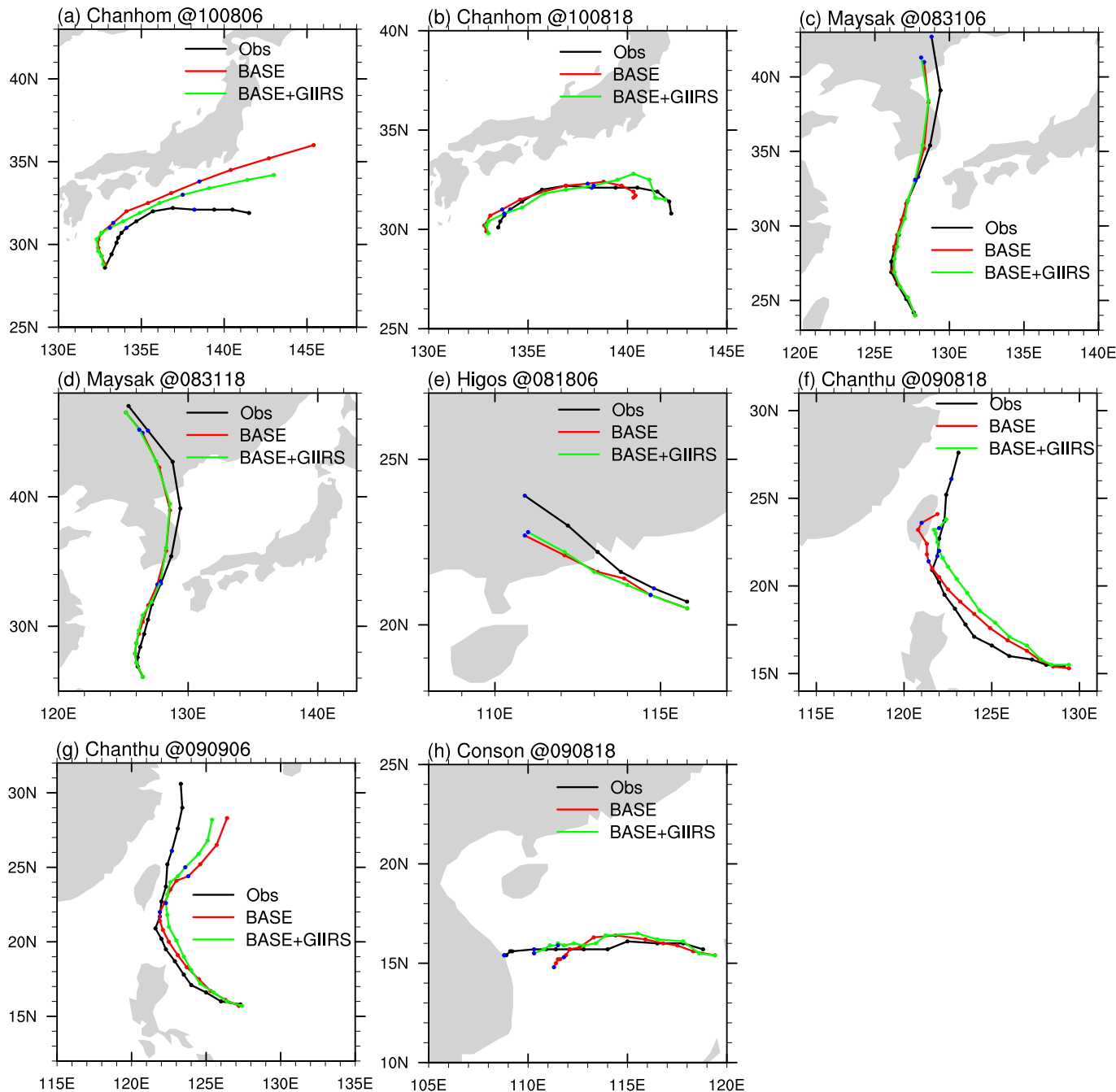


Fig. 2. TC track forecasts of BASE (red line) and BASE+GIIRS (green line) verified against the best-track data (black line) for the eight cases. Blue dots for each track denote the period for the verification of accumulated precipitation in Fig. 14. (For interpretation of the references to colour in this figure legend, the reader is referred to the web version of this article.)

verification for the wind forecast fields uses the Global Data Assimilation System (GDAS) data at a 0.25° resolution at NCEP. The precipitation forecast is verified against the 24-h accumulated precipitation product at a 0.5° resolution from NOAA Climate Prediction Center (CPC).

4. TC track forecasts

4.1. Impact of GIIRS retrieval on TC track forecasts

TC track forecasts are evaluated as a crucial metric of the TC prediction skill. Fig. 2 compares the typhoon track forecasts between BASE (green line) and BASE+GIIRS (red line) verified against the best track

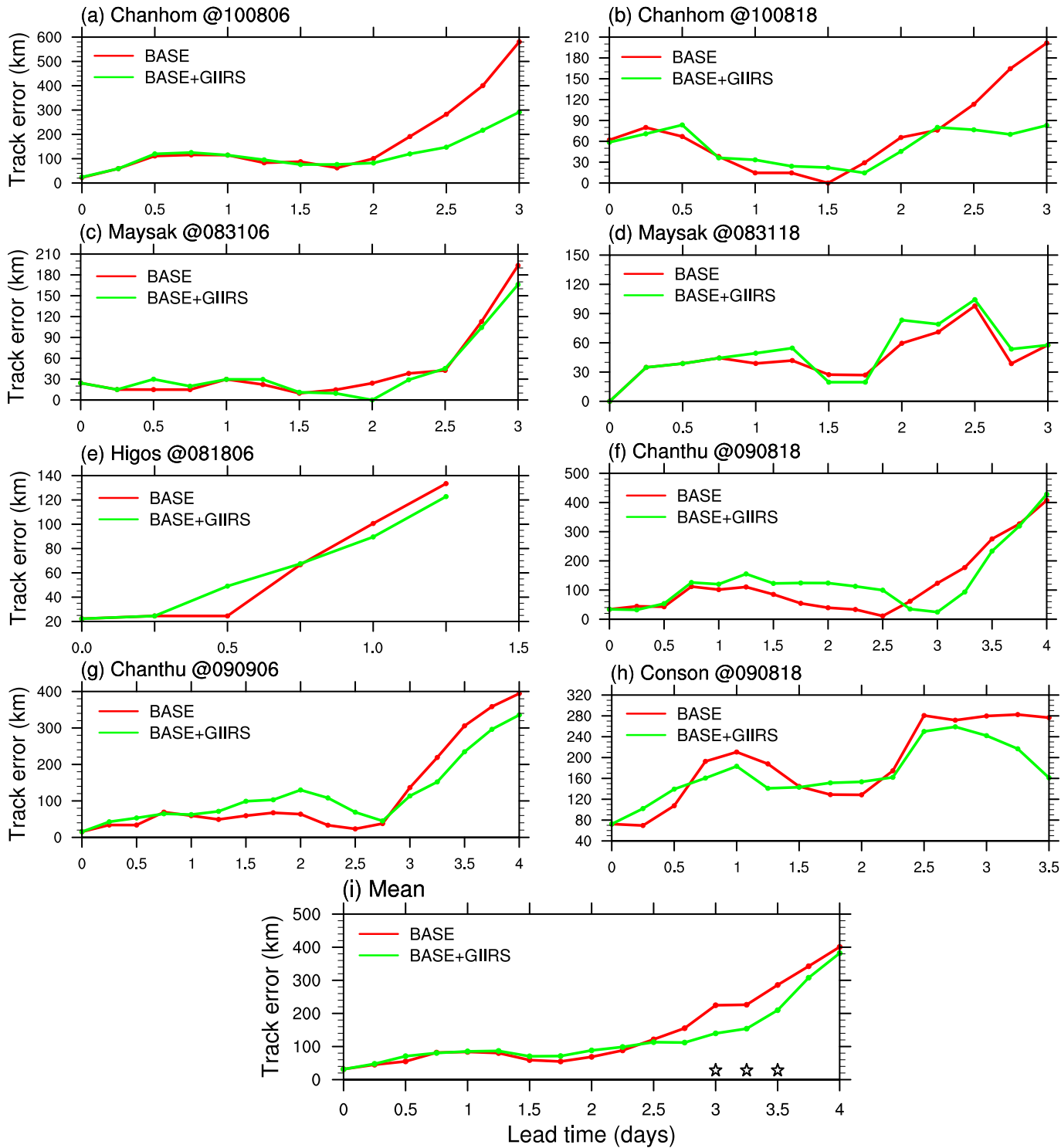


Fig. 3. Tropical cyclone track forecast errors (units: km) for BASE (red) and BASE+GIIRS (green) verified against the best-track forecast for the eight cases. Black stars in Fig. 3*i* indicate statistically significant differences between samples at a 0.05 level. (For interpretation of the references to colour in this figure legend, the reader is referred to the web version of this article.)

(black line) for the eight cases. It is shown that BASE+GIIRS presents better typhoon track forecasts than BASE mainly beyond two days for five out of eight cases (Fig. 2a, b, f, g, and h), including typhoons Chan-hom, Chanthu, and Conson. The improvements reach up to 50% at day 3 for typhoon Chan-hom (Fig. 3a, b) and at day 3.5 for typhoon Conson (Fig. 3h). Noticeably, the TC track forecast with the GIIRS retrieval assimilated in Case 6 accurately suggests that typhoon Chanthu will not make landfall in Taiwan in contrast to BASE (cf. Fig. 2f, green and red curves). By contrast, BASE and BASE+GIIRS have similar TC track forecasts in the other three cases for typhoons Maysak and Higos (see Figs. 2c–e and 3c–e). Note that typhoon Higos has a relatively short lifetime and has already started to decay after making landfall on day 1 (Fig. 2e). The limited DA impact of the GIIRS temperature retrieval for typhoon Maysak can be attributed to the relatively more skillful track forecasts of BASE (cf. Fig. 2c, d and 2a, b) with a more accurate FG field (see Section 4.2b). On average, BASE+GIIRS shows lower TC track forecast errors than BASE beyond 2.5 days despite their similar skill before that (Fig. 3i). The reduction of the mean track errors reaches nearly 100 km at 3 to 3.5 days which is statistically significant at the 0.05 level of the paired *t*-test.

4.2. Mechanisms

The changes in the TC track forecasts of BASE+GIIRS from BASE are attributed to the additional assimilation of the GIIRS temperature retrieval in the initial analysis. It is therefore necessary to examine the influence of the temperature retrieval from GIIRS on TC analysis fields. Considering that the assimilation of the GIIRS temperature profile has a significant impact on the TC track forecast of typhoon Chan-hom, but exerted a very limited influence on typhoon Maysak (cf. Cases 1 and 3 in Fig. 2), the following results show how the assimilation of the GIIRS retrieval influences the TC analysis and prediction by analyzing and comparing these two cases.

4.2.1. Distribution of observations

Before evaluating the impact of the assimilated GIIRS retrieval from FY-4A, we compared the distributions of the operational observations and the GIIRS temperature retrieval assimilated in BASE+GIIRS within the regional domain (i.e., D02) of this study. Fig. 4 shows the mid-level (400–700 hPa) distribution of the assimilated operational observations within D02 for typhoons Chan-hom (Fig. 4a) and Maysak (Fig. 4b) initialized at 0600 UTC on October 8 and 0600 UTC on August 31 (i.e., Cases 1 and 3). Their respective 10-m wind amplitude fields of FG (shading) are given as references. Only rare observations are available for the operational typhoon assimilation and almost all are located far

from the typhoon vortex. It is expected that these observations will only have a reasonably limited influence on typhoon track forecasts.

Fig. 5 shows the distribution of the assimilated temperature retrieval data within 400–700 hPa for the same two cases as Fig. 4. Compared with the operational observations, the GIIRS data from the FY-4A satellite provide a much denser observation network (compare Figs. 5 and 4), covering almost the complete environment of typhoons Chan-hom and Maysak. Nevertheless, the areas near the vortex have fewer observations than the wider environment, probably as a result of the large uncertainties in the retrieval in this area caused by the concentration of clouds on the top of TCs (Li et al., 2021). This is a widely recognized challenge in the use of all-sky satellite data caused by the strong nonlinearity of cloud-affected radiance in dynamic and thermodynamic atmospheric profiles (e.g., Zou et al., 2015; Minamide and Zhang, 2018; Zhang et al., 2018). The lack of near-eyewall observations may possibly explain the limited impact of assimilating the GIIRS retrieval in forecasts of TC intensity.

We calculated the number of temperature retrieval observations from GIIRS assimilated within different vertical layers of D02 for each case (Fig. 6). Fig. 6 shows that there were a large number of retrieval observations (O(4) to O(5)) for all the eight cases across different layers from the surface to the upper troposphere within the six-hour DA window. The number of observations for each case all exceeds 50,000, and the maximum reaches almost 180,000 for Case 1 of typhoon Chan-hom. The layer between 250 and 400 hPa has relatively fewer observations, with only about 25% of the layer above (100–250 hPa). This is probably because the 250–400 hPa layer corresponds to the region of convective cloud at the top of typhoons where the retrieval algorithm has a large sensitivity and thus produces less accurate observations (see also Fig. 5). The relatively high number of observations within the 100–250 hPa layer may be attributed to the greater effectiveness of the retrieval algorithm in the clear sky regions above the clouds.

4.2.2. Fitting of FG and analyses to observations

Effective assimilation should make the analysis closer to the truth or independent verifying observations relative to the FG. We compared the fitting of the FG before assimilation and the analysis after assimilation to the GIIRS retrieval because there were no independent observations for verification. Fig. 7a, b show the absolute differences in the assimilated retrieval observations ("O") between 400 and 700 hPa from the FG and analysis results ("B" and "A", respectively) projected onto the observation space for typhoon Chan-hom at 0600 UTC on October 8 (i.e., |O-B| and |O-A|). The temperature analysis after assimilating the GIIRS retrieval has an overall better fit with the observations, especially in the environment to the northwest and southwest of the TC vortex (cf. Fig. 7a

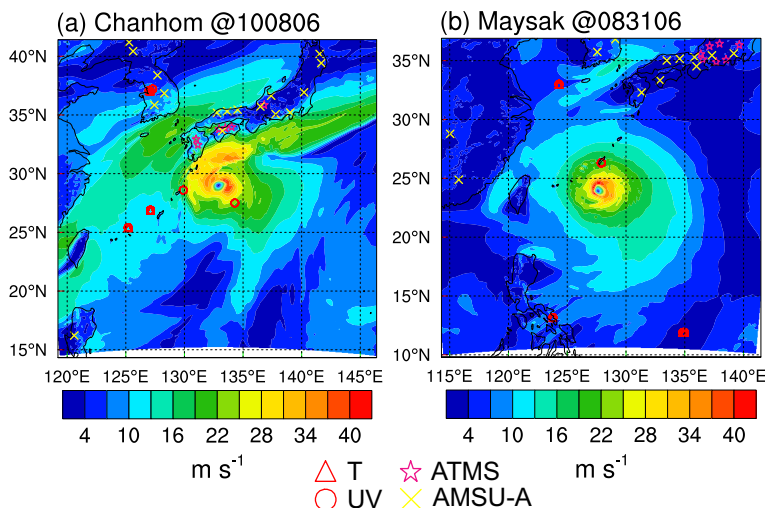


Fig. 4. Distribution of the operational observations assimilated within 400–700 hPa of D02 for typhoon Chan-hom at 0600 UTC on October 8 and typhoon Maysak at 0600 UTC on August 31 overlaid on the 10-m surface wind amplitude field of FG (shading) at the same valid time. The observations include temperature (red triangles) and wind (red circles) from conventional observations and radiance observations from the ATMS (pink stars) and AMSU-A (yellow crosses) satellites. (For interpretation of the references to colour in this figure legend, the reader is referred to the web version of this article.)

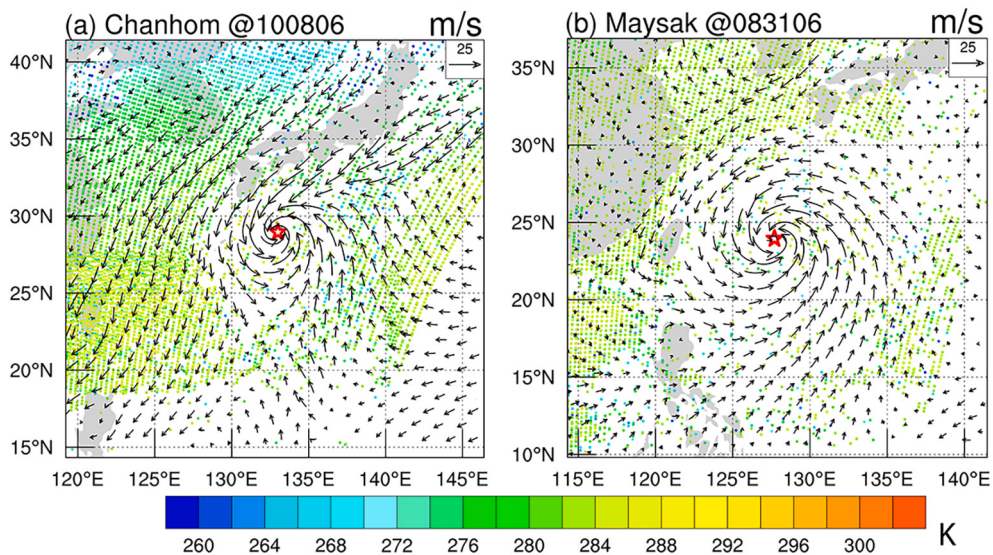


Fig. 5. Distribution of the temperature retrieval observations from GIIRS assimilated within 400–700 hPa of domain D02 for typhoon Chan-hom at 0600 UTC on October 8 and typhoon Maysak at 0600 UTC on August 31 overlaid by the 10-m surface wind field (vectors) of FG at the same valid time. Red stars represent the TC center. (For interpretation of the references to colour in this figure legend, the reader is referred to the web version of this article.)

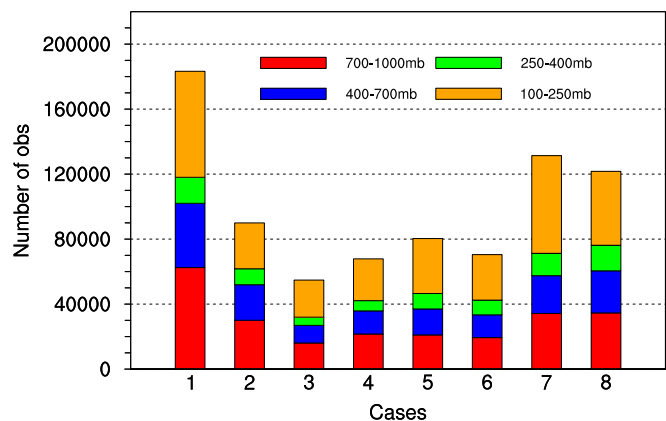


Fig. 6. Number of GIIRS temperature retrieval observations assimilated in different layers of D02.

and b). Quantitatively, the root-mean-square (RMS) differences within the 400–700 hPa layer of D02 change from 1.24 to 0.9 K after assimilation, an almost 25% reduction. This implies that a more accurate analysis field can be obtained for the temperature by assimilating the temperature retrieval from GIIRS, especially in the TC environmental region.

As a comparison, Fig. 7c, d show the same as Fig. 7a, b, but for typhoon Maysak at 0600 UTC on August 31. Their results are qualitatively consistent. However, the improvement in the RMS difference of the observational fitting for analysis is close to 10% (i.e., 1.04 vs. 0.92 K), much less than for typhoon Chan-hom (about 25%). This may be due to the more accurate FG for typhoon Maysak (1.04 K error relative to the 1.24 K for typhoon Chan-hom). The RMS of $|O-A|$ is smaller than that of $|O-B|$ for all cases (Table 3) and the relative reduction ranges from 7% to 27% with a mean value of 18.6%. Overall, the results in Fig. 7 and Table 3 demonstrate the effectiveness of assimilating the GIIRS retrieval to augment the initial temperature analysis.

4.2.3. Initial steering flow

It is widely understood that the movement of TCs is dominantly governed by the steering flow. The steering flow of TCs is generally defined as the mean wind vector averaged over the environment of the

TC within a certain radius in the mid-troposphere. Because there was no direct assimilation of wind observations in our study, it is important to investigate how the momentum field (or the wind field) reacts to an increment in the initial temperature fields.

Fig. 8a shows the steering flow at different levels in the initial conditions of BASE (red arrows) and BASE+GIIRS (green arrows) of typhoon Chan-hom at 0600 UTC on October 8 and their difference in steering flow (blue arrows). The steering flow is calculated by averaging the 500 hPa wind vectors within a $1000 \times 1000 \text{ km}^2$ domain centered at the TC center following Wu et al. (2014). This shows that the initial steering flows of the two experiments in the mid-troposphere (about 500 hPa) both point to the northeast and turn to the north in the upper and lower levels. Nonetheless, BASE+GIIRS has a nearly 1 m s^{-1} southward increment in the steering flow (blue arrows) at 500 hPa and adjacent levels relative to BASE, which is consistent overall with the southerly shift in the TC track in BASE+GIIRS (Fig. 2a).

We further analyzed how the assimilation of temperature retrieval observations resulted in the southward increment of the initial steering flow in BASE+GIIRS relative to BASE. Fig. 9 shows the differences (shading) in the average temperature within the atmospheric column above 500 hPa (Fig. 9a) and the geopotential height (GH) at 500 hPa (Fig. 9b) between the initial analyses of BASE+GIIRS and BASE for typhoon Chan-hom. The differences are overlaid by the temperature and GH analyses (purple contours) of BASE at 500 hPa, respectively, for reference. The differences in the GH at 500 hPa and the average temperature above this height were roughly negatively oriented, especially in the near-vortex environment within a 500-km radius (red circle) of the TC center (red star). This can be explained by the hydrostatic relationship in the vertical direction—that is, the colder (warmer) air column corresponding to the higher (lower) pressure at the bottom. We highlight the red transect because it comprises the entrance and outlet of the large-scale trough in which typhoon Chan-hom is embedded (Fig. 9b, c). Adjustment of the GH in BASE+GIIRS along the given transect (Fig. 9b) with the additional assimilation of the retrieval observations leads to the change in the meridional wind (shading) associated with the steering flow in Fig. 9c.

The cross-variable relationship between the thermodynamic and momentum variables can be better illustrated by the vertical zonal section along the transect (red straight line) in Fig. 9 (see Fig. 10). The differences in the vertically averaged temperature and GH between BASE and BASE+GIIRS have a close to -0.4 negative correlation (cf.

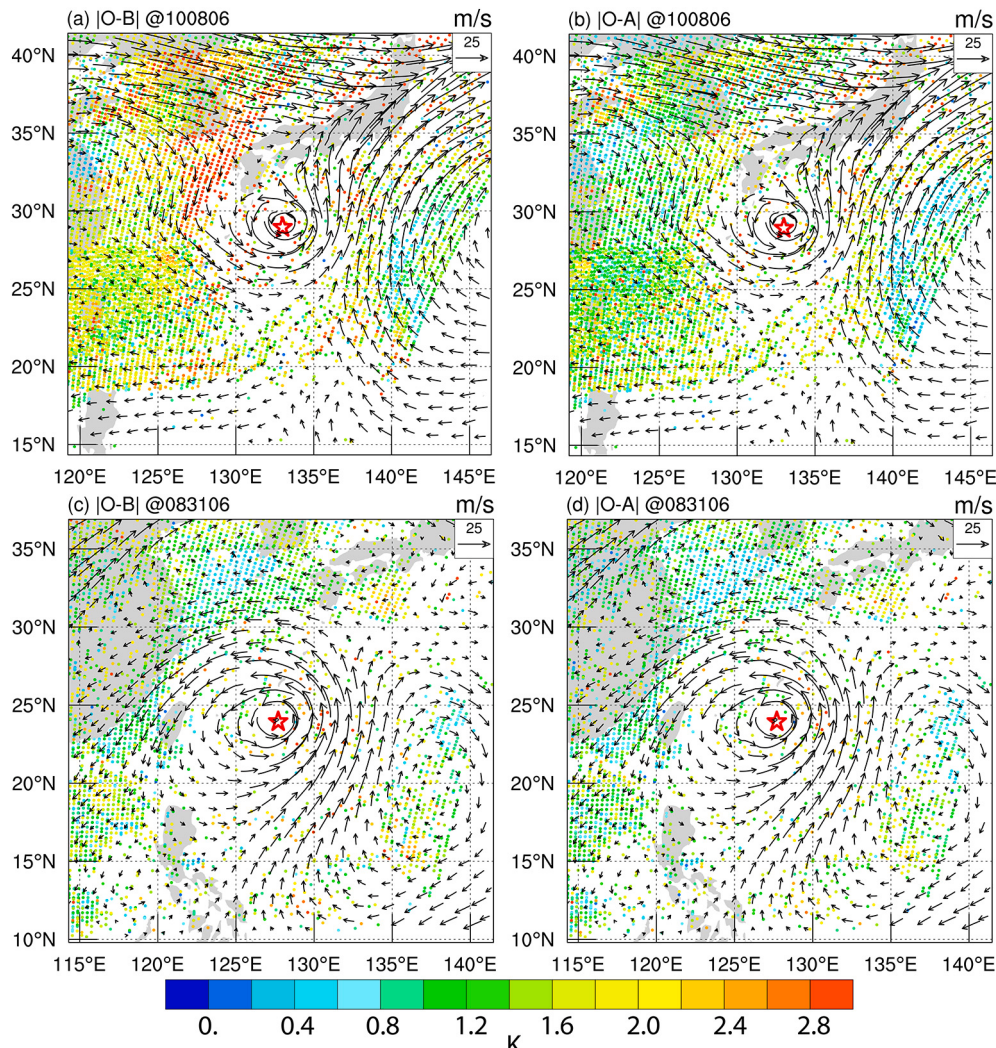


Fig. 7. Absolute differences (colored dots) in the fitting of (a) first guess and (b) the analysis to the assimilated temperature retrieval from GIIRS within the 400–700 hPa layer of D02 overlaid by the 500 hPa wind field (vectors) in FG for typhoon Chan-hom at 0600 UTC on October 8. Fig. 7(c)-(d) are the same as Fig. 7(a)-(b), but for typhoon Maysak at 0600 UTC on August 31.

Table 3

RMS of |O-B| and |O-A| averaged over D02 between 400 and 700 hPa for all cases and the relative reduction (%) of |O-A| from |O-B|.

Case No.	1	2	3	4	5	6	7	8	Mean
O-B	1.24	1.22	1.04	1.02	1.08	1.36	1.20	1.24	1.18
O-A	0.90	0.96	0.92	0.88	1.00	0.99	1.08	0.94	0.96
Relative Reduction (%)	27.4	21.3	11.5	13.7	7.4	27.2	10.0	24.2	18.6

Fig. 10a and b). This indicates the influence of assimilating temperature observations on the GH analysis through the hydrostatic relationship. As a response to the adjustment of the GH, the meridional wind presents a negative difference in the northwestern environment of typhoon Chan-hom near the mid-troposphere (i.e., near label A in Fig. 10c), corresponding to an intensification of the southerly wind. The meridional wind also presents negative differences in the northern and northeastern environment of typhoon Chan-hom (i.e., near labels B and C in Fig. 10c, respectively), corresponding to the weakening of the northerly winds. Such differences in the meridional wind imply a southward difference in the initial steering flow between BASE+GIIRS and BASE, as suggested in Fig. 8a. By contrast, the differences in the vertically averaged temperature, GH, and wind component between BASE and BASE+GIIRS are much smaller for typhoon Maysak (not shown), which is consistent with the conclusions from Fig. 7.

5. Impact of GIIRS retrieval on wind and rainfall forecasts

Section 4.2c introduces the influence of assimilating temperature retrieval observations from FY-4A on the initial TC steering flow (Fig. 8a) and its mechanism (Figs. 9 and 10). Noticeably, the change in the initial steering flow also influences the steering flow in subsequent forecasts of typhoon Chan-hom (Fig. 8b). The differences in the steering flow within the 400–600 hPa layer between BASE+GIIRS and BASE remain a southward component from 12 to 36 h despite being small within 24 and 36 h. Later, the southward difference in the steering flow amplifies and transfers to the west, where it is dominated by a westerly component exceeding 5 m s⁻¹ after 60 h. This result is consistent with the more southward and slower movement of the TC track in BASE+GIIRS relative to BASE, leading to a more accurate TC track forecast.

It is crucial to improve the wind forecast near coasts when TCs are

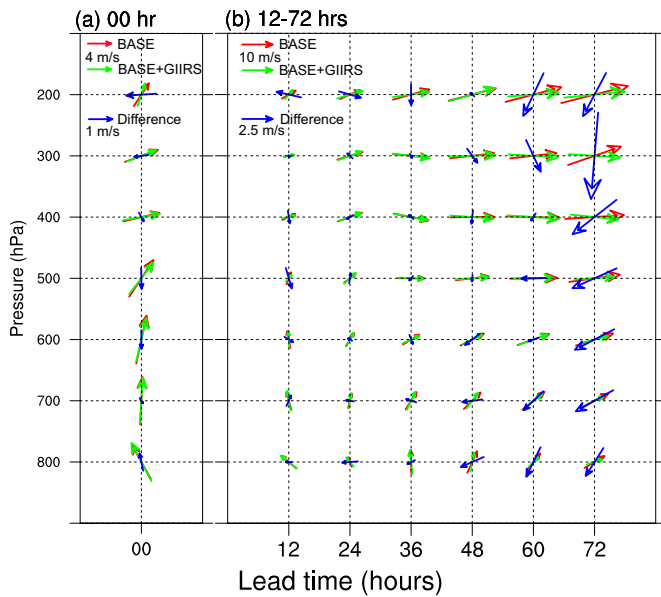


Fig. 8. Steering flow of BASE (red) and BASE+GIIRS (green) and their differences (blue) at the (a) initial time and (b) forecast lead times for typhoon Chan-hom initialized at 0600 UTC on October 8. (For interpretation of the references to colour in this figure legend, the reader is referred to the web version of this article.)

approaching landfall. Fig. 11 shows the 2.5-day wind field forecasts at 500 and 1000 hPa for the BASE and BASE+GIIRS experiments verified against the GDAS initial analyses valid at the same time for typhoon Chan-hom initialized at 0600 UTC on October 8. At the 2.5-day forecast lead time, typhoon Chan-hom is only about 200 km away from the south-central coast of Japan (Fig. 11a, d). Both BASE and BASE+GIIRS capture the easterly low-pressure trough in the mid-troposphere (500 hPa) of typhoon Chan-hom (cf. Fig. 11a and b, c). However, unlike BASE, the wind forecast of BASE+GIIRS shows a complete vortex embedded in the trough at 500 hPa (near the purple cross in Fig. 11c), the same as in the observations (cf. Fig. 11c and a). If we focus on the $1000 \times 1000 \text{ km}^2$ domain (purple square) surrounding the observed TC

center, BASE+GIIRS clearly shows a better wind forecast than BASE at mid-levels—for example, the smaller areas of green shading (cf. Fig. 11b and c). The RMS error within the specified domain at 500 hPa reduces to 8.7 from 9.8 m s^{-1} , a nearly 10% improvement. The near-surface (1000 hPa, Fig. 11e and f) realizes an even larger improvement in the wind forecasts within the specified domain—that is, a nearly 33% reduction in the RMS error ($12.3 \text{ vs. } 7.9 \text{ m s}^{-1}$). BASE+GIIRS has a more accurate forecast of the distance between the TC inner core and the coast than BASE (cf. purple cross and star in Fig. 11e and f) and may therefore avoid excessive defensive measures in disaster mitigation.

We also evaluated the RMSE of 1000-hPa wind forecasts in a $1000 \times 1000 \text{ km}^2$ domain surrounding the observed TC center at each lead time for all cases (Fig. 12). It is shown that the sample-mean wind RMSE of BASE+GIIRS and BASE are very close within the first 2.5 days. However, BASE+GIIRS presents about $1\text{--}2 \text{ ms}^{-1}$ lower RMSEs beyond 2.5 days (black line) though the differences are not statistically significant due to the limited number of cases. The performance of individual cases also shows that about half of the cases for BASE+GIIRS present lower RMSE within 2.5 days, and most cases of BASE+GIIRS outperform BASE beyond 2.5 days. In addition, the wind forecast RMSE is closely related to the performance of the TC track forecast in each case (cf. Figs. 12 and 3). An evaluation based on more TC cases is warranted to verify the robustness of the improved wind forecasts by assimilating the temperature retrieval from the FY-4A GIIRS.

We further evaluated the forecast skill of typhoon-induced precipitation on land. Fig. 13 shows the forecasts of the 24-h cumulative precipitation from 30- to 54-h lead times for typhoon Chan-hom initialized at 0600 UTC on October 8 for BASE (Fig. 13b) and BASE+GIIRS (Fig. 13c). The verifying data (Fig. 13a) use the global unified gauge-based analysis of daily precipitation from the NOAA Climate Prediction Center at a resolution of 0.5° within the same period. The observations (Fig. 13a) show that the main precipitation area on land associated with the approaching typhoon (red stars) is concentrated on the south-central coast of Japan between 34° and 36° N with two precipitation centers (highlighted by red boxes). The BASE and BASE+GIIRS forecasts roughly capture the position of the two major centers of observed precipitation but overpredict the strength, especially the eastern center (cf. Fig. 13b, c and a). Nonetheless, BASE+GIIRS presents a much smaller area with precipitation $>120 \text{ mm}$ than BASE for the eastern center, which is closer to the observations. It is associated with

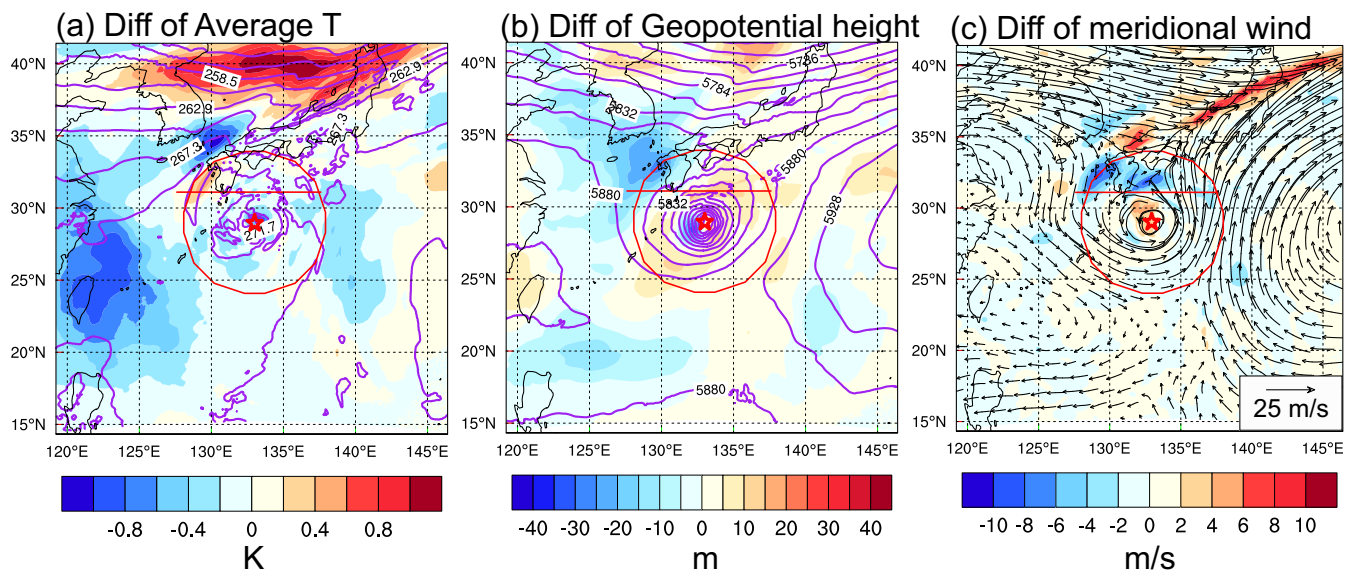


Fig. 9. Differences (shading) in (a) the average temperature within the atmospheric column above 500 hPa, (b) the geopotential height and (c) meridional wind at 500 hPa between the initial analyses of BASE+GIIRS and BASE for typhoon Chan-hom at 0600 UTC on October 8. The overlaid are the (a) temperature, (b) GH, and (c) wind fields in the analysis of BASE at 500 hPa.

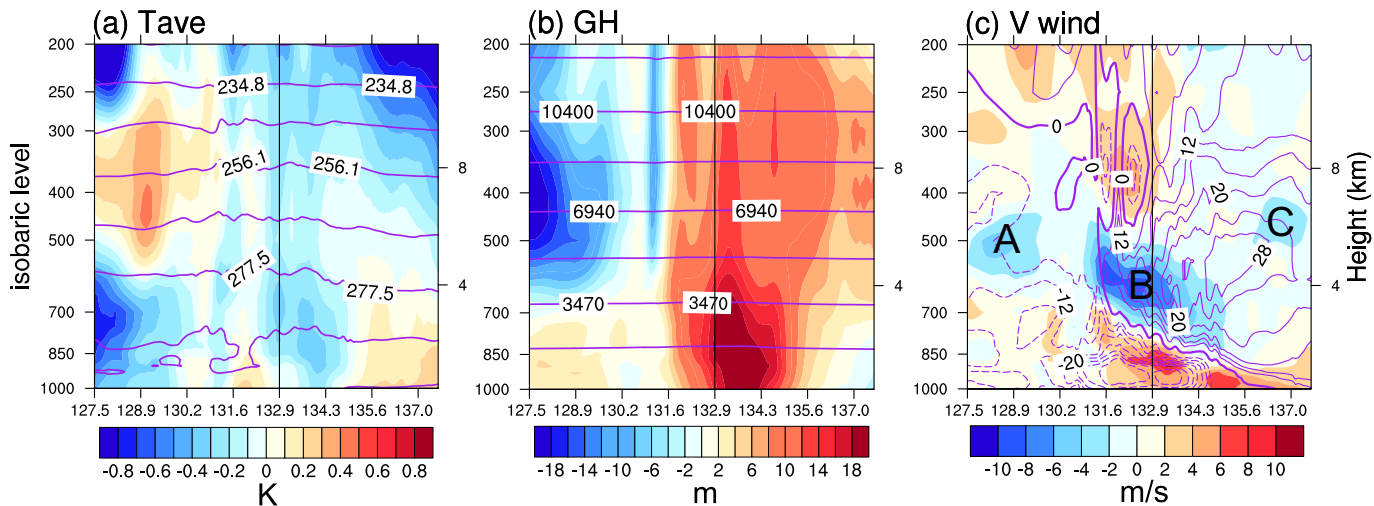


Fig. 10. Vertical cross-section (along the red straight line in Fig. 10) of the differences (shading) in (a) the average temperature within the above atmosphere column, (b) the geopotential height, and (c) the meridional wind between the initial analyses of BASE+GIIRS and BASE for typhoon Chan-hom at 0600 UTC October 8. The overlaid are the (a) temperature, (b) geopotential height and (c) meridional wind in the analysis of BASE at 500 hPa. The black line denotes the longitude of the center of the typhoon. (For interpretation of the references to colour in this figure legend, the reader is referred to the web version of this article.)

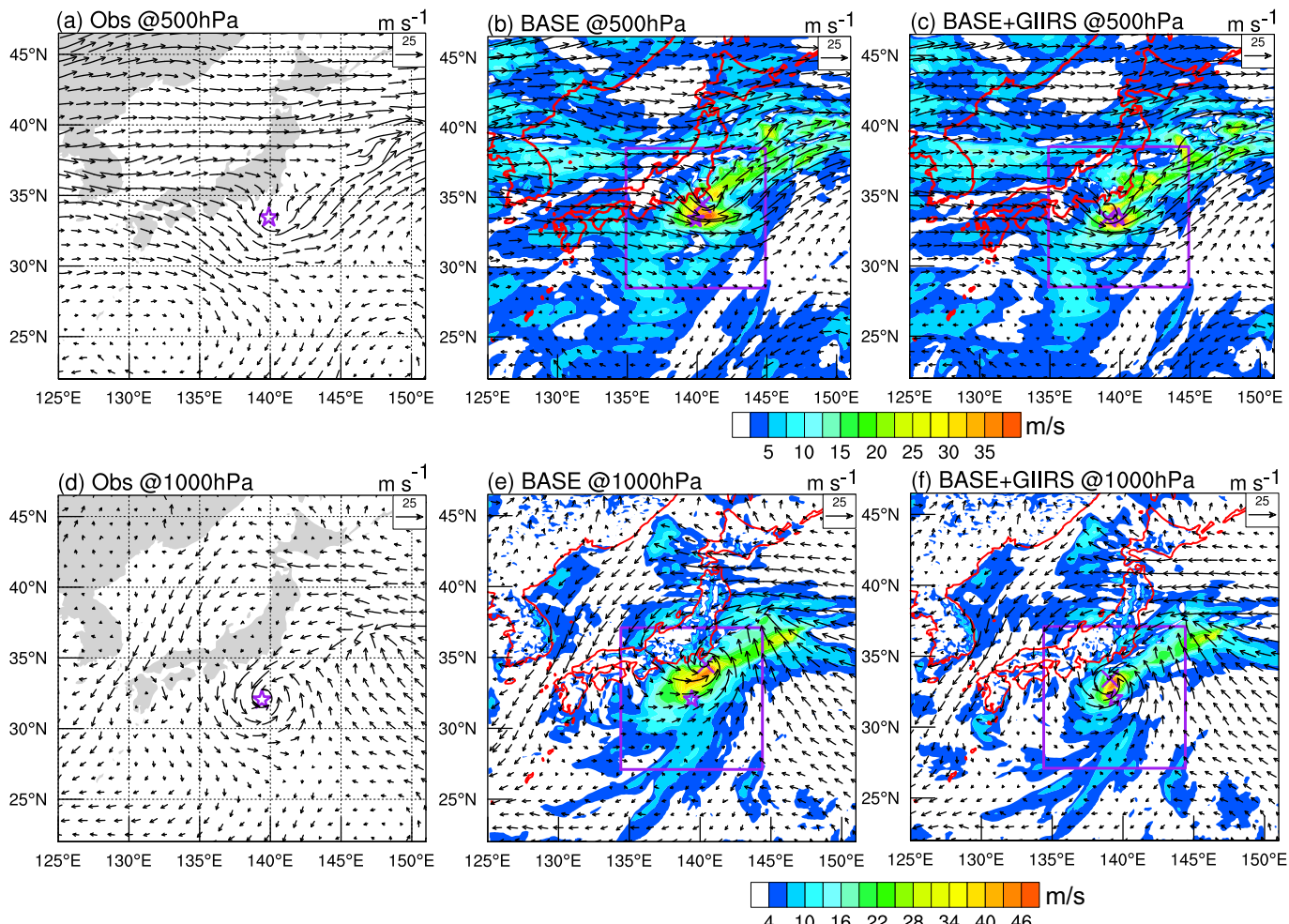


Fig. 11. 2.5-day wind field (vectors) forecasts and wind amplitude error (shading) at 500 hPa of the (b) BASE and (c) BASE+GIIRS experiments verified against (a) the GDAS initial analyses valid at the same time for typhoon Chan-hom initialized at 0600 UTC on October 8. Purple stars and crosses represent the observed and forecast TC centers, respectively. **Fig. 11(d)-(f)** are the same as 11(a)-(c), but for 1000 hPa level. (For interpretation of the references to colour in this figure legend, the reader is referred to the web version of this article.)

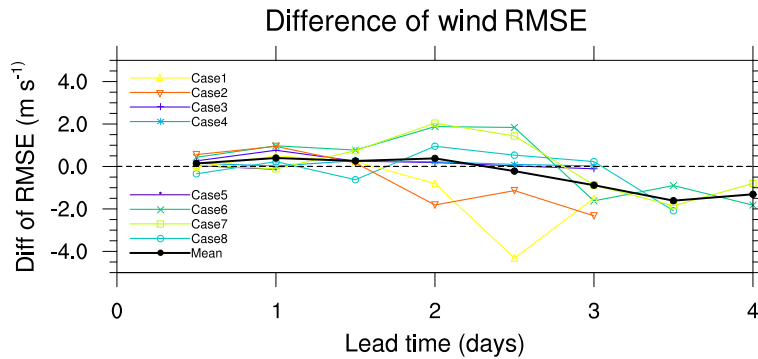


Fig. 12. Differences of the 1000-hPa wind forecast RMSE of BASE+GIIRS from BASE (i.e., BASE+GIIRS minus BASE) in a 1000×1000 km 2 domain surrounding the observed TC center at each lead time for all cases and their mean (black line).

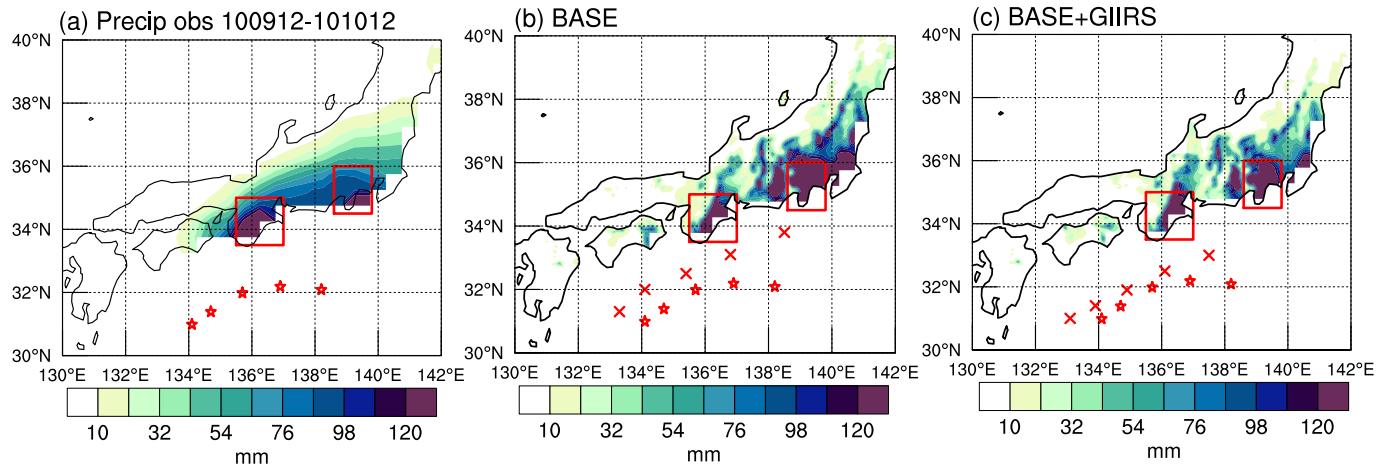


Fig. 13. Forecasts of the 24-h cumulative precipitation from 30- to 54-h lead times for (b) BASE and (c) BASE+GIIRS for typhoon Chan-hom initialized at 0600 UTC on October 8 and (a) the verifying observations. The observations use the global unified gauge-based analysis of daily precipitation from the NOAA Climate Prediction Center at 0.5° resolution. The red stars and crosses represent the observed and forecast TC centers, respectively, within the verification period. (For interpretation of the references to colour in this figure legend, the reader is referred to the web version of this article.)

the more accurate TC track forecast in BASE+GIIRS with the assimilation of the vertical temperature retrieval (cf. cross and star in Fig. 13c).

The predictions of the 24-h cumulative precipitation on land are quantitatively evaluated for all cases using the classic threat score (TS) while TCs are approaching or in the process of landfall (see Fig. 2 and Table 1 for the period of verification). The TS measures the fraction of observed events (24-h cumulative precipitation >50 mm in this study) that was correctly predicted within a specified domain (a 1000×1000 km 2 domain surrounding the observed TC center in this study). TS is a positive-oriented metric, TS = 1 means a perfect forecast and TS = 0 means a useless forecast.

Fig. 14 shows the TS for all cases and their sample-mean performance. The better rainfall forecast of BASE+GIIRS in Case 1 in Fig. 13 can be further confirmed by the improved quantitative TS in Fig. 14, with an about 9.4% higher score. Five out of the eight cases show improved prediction skill of BASE+GIIRS in 24-h cumulative precipitation compared to BASE. This may be associated with the more accurate TC track forecasts of BASE+GIIRS. The sample-mean TS of BASE+GIIRS is about 7.6% higher than that of BASE. The assimilation of GIIRS retrieval could also influence the forecast of TC precipitation by modulating the dynamic and thermodynamic evolution of TC inner structures. However, this is not analyzed in detail in this study and will be carefully examined in a case study in future work.

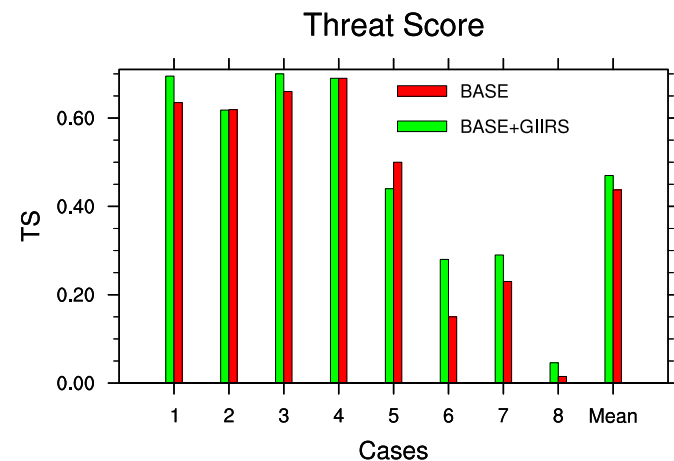


Fig. 14. Threat score of the prediction of 24-h cumulative precipitation (> 50 mm) for BASE (red) and BASE+GIIRS (green) for all cases and their mean performance. (For interpretation of the references to colour in this figure legend, the reader is referred to the web version of this article.)

6. Conclusions and discussion

Although the observing network for tropical cyclones has been extensively augmented in recent decades, movable observing platforms that can monitor TCs with spatial and temporal continuity are still lacking. High spectral resolution infrared sounders onboard geostationary satellites—for example, the GIIRS on the FY-4A geostationary satellite—offer such a possibility. Using this, a series of field campaigns of targeting observation based on the CNOP sensitivity were carried out for five typhoons (Chan-hom, Maysak, Higos, Chanthu, and Conson) in the western North Pacific Ocean in the summers of 2020 and 2021. The FY-4A GIIRS was committed to a one-day continuous scan of the vortex and the surrounding environment for individual typhoons. The atmospheric temperature profile data retrieved from the GIIRS were assimilated to evaluate their impacts on TC forecasts using a regional high-resolution HWRF model.

The main results indicate that the assimilation of the temperature profile retrieval reduces the track forecast errors of typhoons beyond 2.5 days by up to 100 km on average which is statistically significant at 3 to 3.5 days. Especially, the track error reduction for Chan-hom and Conson can reach up to 50% at about day 3 with the additional assimilation of GIIRS retrieval observations. By contrast, the assimilation impact on Maysak and Higos was limited. Such a case-dependent performance is mainly related to the TC simulation performance in the FG field. By examining the fitting of the FG field and analysis to the retrieval observations, all the typhoons showed a reduction in fitting errors after assimilating the GIIRS retrieval. However, typhoon Chan-hom had a poorer TC simulation in FG than typhoon Maysak and therefore showed a greater improvement in the tropical cyclone track by assimilating the retrieval.

A detailed analysis showed that the analysis increment of temperature influenced the initial momentum variables (i.e., the geopotential height and wind), probably through the hydrostatic relationship. The initial steering flow in the analysis fields of typhoon Chan-hom was then modified to be closer to the observations, which contributed to the improved forecast of the TC track. The more accurate TC initial conditions also contributed to the improved wind forecasts in the near-coast areas at surface levels and the precipitation forecasts on land in terms of the averaged performance for all cases.

This study demonstrates the benefit of assimilating satellite retrieval of the temperature profile from the GIIRS onboard the FY-4A satellite in improving the forecasts of the TC tracks, winds and precipitation. These positive impacts of assimilation indirectly show the effectiveness of the retrieval algorithm for the GIIRS radiance in resolving the vertical atmospheric temperature profile. So far, satellite-based atmospheric motion vector observations have made positive contributions to the prediction of the TC track and intensity. The GIIRS onboard the FY-4A satellite provides valuable supplementary observations to the thermodynamic structures of TCs and the surrounding environment. How the assimilation of the thermodynamic profile retrieval modulates the evolution of the moisture thermodynamic processes and rainband of TCs on the convection scale will be studied in future work.

Although the weak analysis increment of temperature and wind can be seen near the TC eyewall of Chan-hom (Fig. 9), the forecasts of TC intensity overall show limited impact from assimilating the temperature retrieval of the GIIRS. This may be associated with the sparse observations within the TC vortex as a result of the high sensitivity of the retrieval algorithm in cloudy regions. The development of more accurate all-sky retrieval algorithms is crucial to enhance the utility of the GIIRS observations in the prediction of TC intensity. On the other hand, the limited impact of assimilation on TC intensity may be associated with the horizontal resolution of the GIIRS data at about 16 km, which may not be sufficiently high to resolve the thermodynamic structure near the TC warm core. The GIIRS onboard the FY-4B has been upgraded with higher horizontal resolution (12 km) and calibration precision, which facilitates improved scan of the TC warm core. This may benefit the

initialization of the TC near-eyewall structure and intensity and their prediction.

Data availability

The operational observations assimilated in this study are provided by Dr. Jincheng Wang. The global control forecast product of GFS and the verification data of GDAS can be downloaded from the Research Data Archive at <https://rda.ucar.edu/datasets/ds084.1/>. The global ensemble forecast product of GEFS at NCEP are provided by Dr. Hong Li at Shanghai Typhoon Institute of CMA, and can also be downloaded from NCEP operational product inventory of GEFS at <https://www.nco.ncep.noaa.gov/pmb/products/gens/>. The Typhoon best-track data can be downloaded from the data archive center at https://tcdatalab.typhoon.org.cn/zjljsj_zlhq.html. The precipitation product for verification uses the global unified gauge-based analysis downloaded from NOAA Climate Prediction Center (CPC) at <https://psl.noaa.gov/data/gridded/data.cpc.globalprecip.html>.

CRediT authorship contribution statement

Jie Feng: Conceptualization, Methodology, Investigation, Writing – original draft, Writing – review & editing. **Xiaohao Qin:** Writing – original draft, Writing – review & editing. **Chunqiang Wu:** Data curation. **Peng Zhang:** Resources. **Lei Yang:** Resources. **Xueshun Shen:** Resources. **Wei Han:** Resources. **Yongzhu Liu:** Resources.

Declaration of Competing Interest

The authors declare that they have no known competing financial interests or personal relationships that could have appeared to influence the work reported in this paper.

Data availability

Data will be made available on request.

Acknowledgments

The authors are grateful to Dr. Jincheng Wang (Numerical Weather Prediction Center of CMA) for providing the operationally assimilated observations in the global GRAPES. The global ensemble forecast data of GEFS at NCEP used to run the regional background ensemble were kindly provided by Dr. Hong Li (Shanghai Typhoon Institute, CMA). Discussions with Profs. Wei Huang, Bin Mu, Shijin Yuan, Feng Zhang, and Drs. Bingqiang Sun, Xinyan Lyu are gratefully acknowledged. This study was jointly supported by the funding of the Science and Technology Commission of Shanghai Municipality, China (20dz1200700) and the Innovation Research Foundation of Fudan University in China (Grant No. IDH2318003/001/013).

References

- Alpert, J.C., Kumar, V.K., 2007. Radial wind super-obs from the WSR-88D radars in the NCEP operational assimilation system. Mon. Weather Rev. 135, 1090–1108. <https://doi.org/10.1175/MWR3324.1>.
- Biswas, M.K., Carson, L., Newman, K., Bernardet, L., Kalina, E., Grell, E., Frimel, J., 2017. Community HWRF Users' Guide V3.9a, 160 pp.
- Bloom, H.J., 2001. The Cross-track Infrared Sounder (CrIS): A sensor for operational meteorological remote sensing. In: IEEE 2001 International Geoscience and Remote Sensing Symposium, vol. 3. IEEE, pp. 1341–1343. <https://doi.org/10.1109/IGARSS.2001.976838>.
- Chahine, M.T., Coauthors, 2006. AIRS: improving weather forecasting and providing new data on greenhouse gases. Bull. Amer. Meteor. Soc. 87, 911–926. https://doi.org/10.1175/BA_MS-87-7-911.
- Clerbaux, C., Coauthors, 2007. The IASI/MetOp I Mission: first observations and highlights of its potential contribution to GMES. Space Res. Today 168, 19–24. [https://doi.org/10.1016/S0045-8732\(07\)80046-5](https://doi.org/10.1016/S0045-8732(07)80046-5).

- Di, D., Li, J., Han, W., Bai, W., Wu, C., Menzel, W.P., 2018. Enhancing the fast radiative transfer model for Fengyun-4 GHIRS by using local training profiles. *J. Geophys. Res. Atmos.* 123, 12583–12596. <https://doi.org/10.1029/2018JD029089>.
- Feng, J., Wang, X.G., 2019. Impact of assimilating upper-level dropsonde observations collected during the TCI field campaign on the prediction of intensity and structure of Hurricane Patricia (2015). *Mon. Weather Rev.* 147, 3069–3089. <https://doi.org/10.1175/MWR-D-18-0305.1>.
- Feng, J., Wang, X.G., 2021. Impact of increasing horizontal and vertical resolution of the hurricane WRF model on the analysis and prediction of Hurricane Patricia (2015). *Mon. Weather Rev.* 149, 419–441. <https://doi.org/10.1175/MWR-D-20-0144.1>.
- Li, J., Liu, H., 2009. Improved hurricane track and intensity forecast using single field-of-view advanced IR sounding measurements. *Geophys. Res. Lett.* 36, L11813. <https://doi.org/10.1029/2009GL038285>.
- Li, J., Wolf, W.W., Menzel, W.P., Zhang, W., Huang, H.L., Achtor, T.H., 2000. Global soundings of the atmosphere from ATOVS measurements: the algorithm and validation. *J. Appl. Meteorol.* 39 (8), 1248–1268.
- Li, J., Geer, A.J., Okamoto, K., et al., 2021. Satellite All-sky Infrared Radiance Assimilation: recent Progress and Future Perspectives. *Adv. Atmos. Sci.* <https://doi.org/10.1007/s00376-021-1088-9>.
- Lu, X., Wang, X.G., 2020. Improving hurricane analyses and predictions with TCI, IFEX field campaign observations, and CIMSS AMVs using the advanced hybrid data assimilation system for HWRF. Part II: observation impacts on the analysis and prediction of Patricia (2015). *Mon. Weather Rev.* 148, 1407–1430. <https://doi.org/10.1175/MWR-D-19-0075.1>.
- Lu, X., Wang, X., Li, Y., Tong, M., Ma, X., 2017a. GSI-based ensemble-variational hybrid data assimilation for HWRF for hurricane initialization and prediction: impact of various error covariances for airborne radar observation assimilation. *Quart. J. Roy. Meteor. Soc.* 143, 223–239. <https://doi.org/10.1002/qj.2914>.
- Lu, X., Wang, X., Li, Y., Tong, M., Tallapragada, V., 2017b. GSI-based, continuously cycled, dual-resolution hybrid ensemble-variational data assimilation system for HWRF: system description and experiments with Edouard (2014). *Mon. Weather Rev.* 145, 4877–4898. <https://doi.org/10.1175/MWRD-17-0068.1>.
- Ma, Z., Li, J., Han, W., Li, Z., Zeng, Q., Menzel, W.-P., et al., 2021. Four-dimensional wind fields from geostationary hyperspectral infrared sounder radiance measurements with high temporal resolution. *Geophys. Res. Lett.* 48 (14) <https://doi.org/10.1029/2021GL093794> e2021GL093794.
- Menzel, P.W., Schmit, T.J., Zhang, P., Li, J., 2018. Satellite based atmospheric infrared sounder development and applications. *Bull. Am. Meteorol. Soc.* 99, 583–603.
- Minamide, M., Zhang, F., 2018. Assimilation of all-sky infrared radiances from Himawari-8 and impacts of moisture and hydrometer initialization on convection-permitting tropical cyclone prediction. *Mon. Weather Rev.* 146, 3241–3258. <https://doi.org/10.1175/MWR-D-17-0367.1>.
- Mu, M., Duan, W.S., Wang, B., 2003. Conditional nonlinear optimal perturbation and its applications. *Nonlin. Processes Geophys.* 10, 493–501.
- Mu, M., Zhou, F., Wang, H., 2009. A method for identifying the sensitive areas in targeted observations for tropical cyclone prediction: Conditional nonlinear optimal perturbation. *Mon. Weather Rev.* 137, 1623–1639.
- Nystrom, R.G., Zhang, F., Munsell, E.B., Braun, S.A., Sippel, J.A., Weng, Y., Emanuel, K. A., 2018. Predictability and dynamics of Hurricane Joaquin (2015) explored through convection-permitting ensemble sensitivity experiments. *J. Atmos. Sci.* 75, 401–424. <https://doi.org/10.1175/JAS-D-17-0137.1>.
- Qin, X.H., Duan, W.S., Chan, P.W., Chen, B.Y., Huang, K.-N., 2022. Effects of dropsonde data in field campaigns on forecasts of tropical cyclones over the western North Pacific in 2020 and the role of CNOP sensitivity. *Adv. Atmos. Sci.* <https://doi.org/10.1007/s00376-022-2136-9>.
- Qin, X.H., Mu, M., 2011. Influence of conditional nonlinear optimal perturbations sensitivity on typhoon track forecasts. *Q. J. Roy. Meteor. Soc.* (138), 185–197.
- Schmetz, J., 2021. Good things need time: progress with the first hyperspectral sounder in geostationary orbit. *Geophys. Res. Lett.* <https://doi.org/10.1029/2021GL096207>, 48, 21.
- Smith Sr., W.L., Coauthors, 2009. Technical note: evolution, current capabilities, and future advance in satellite nadir viewing ultra-spectral IR sounding of the lower atmosphere. *Atmos. Chem. Phys.* 9, 5563–5574. <https://doi.org/10.5194/acp-9-5563-2009>.
- Smith Sr., W.L., Weisz, E., Kireev, S.V., Zhou, D.K., Li, Z., Borbas, E.E., 2012. Dual-regression retrieval algorithm for real-time processing of satellite ultraspectral radiances. *J. Appl. Meteorol. Climatol.* 51 (8), 1455–1476.
- Torn, R.D., Whitaker, J.S., Pegion, P., Hamill, T.M., Hakim, G.J., 2015. Diagnosis of the source of GFS medium-range track errors in Hurricane Sandy (2012). *Mon. Weather Rev.* 143, 132–152. <https://doi.org/10.1175/MWR-D-14-00086.1>.
- Wang, X., 2010. Incorporating ensemble covariance in the Gridpoint Statistical Interpolation (GSI) variational minimization: a mathematical framework. *Mon. Weather Rev.* 138, 2990–2995. <https://doi.org/10.1175/2010MWR3245.1>.
- Wang, F., Li, J., Schmit, T.J., Ackerman, S., 2007. Trade-off studies of a hyperspectral infrared sounder on a geostationary satellite. *Appl. Opt.* 46, 200–209.
- Wang, X., Parrish, D., Kleist, D., Whitaker, J., 2013. GSI 3DVar-based ensemble-variational hybrid data assimilation for NCEP Global Forecast System: single-resolution experiments. *Mon. Weather Rev.* 141, 4098–4117. <https://doi.org/10.1175/MWR-D-12-00141.1>.
- Weng, Y., Zhang, F., 2012. Assimilating airborne Doppler radar observations with an ensemble Kalman filter for convection-permitting hurricane initialization and prediction: Katrina (2005). *Mon. Weather Rev.* 140, 841–859. <https://doi.org/10.1175/2011MWR3602.1>.
- Wu, C.C., Huang, T.-S., Chou, K.-H., 2004. Potential vorticity diagnosis of the key factors affecting the motion of Typhoon Sinlaku (2002). *Mon. Weather Rev.* 132, 2084–2093. [https://doi.org/10.1175/1520-0493\(2004\)132<2084:PVDOTK>2.0.CO;2](https://doi.org/10.1175/1520-0493(2004)132<2084:PVDOTK>2.0.CO;2).
- Wu, T.C., Liu, H., Majumdar, S., Velden, C., Anderson, J., 2014. Influence of assimilating satellite-derived atmospheric motion vector observations on numerical analyses and forecasts of tropical cyclone track and intensity. *Mon. Weather Rev.* 142, 49–71. <https://doi.org/10.1175/MWR-D-13-00023.1>.
- Xian, D., Zhang, P., Gao, L., Sun, R.J., Zhang, H.Z., Jia, X., 2021. Fengyun meteorological satellite products for earth system science applications. *Adv. Atmos. Sci.* 38 (8), 1267–1284. <https://doi.org/10.1007/s00376-021-0425-3>.
- Yang, J., Zhang, Z., Wei, C., Lu, F., Guo, Q., 2017. Introducing the new generation of Chinese geostationary weather satellites, Fengyun-4. *Bull. Amer. Meteorol. Soc.* 98, 1637–1658. <https://doi.org/10.1175/BAMS-D-16-0065.1>.
- Yin, R.Y., Han, W., Gao, Z.Q., Di, D., 2020. The evaluation of FY4A's Geostationary Interferometric Infrared Sounder (GIIRS) long-wave temperature sounding channels using the GRAPES global 4D-Var. *Quart. J. Roy. Meteor. Soc.* 146, 1459–1476. <https://doi.org/10.1002/qj.3746>.
- Yin, R.-Y., Han, W., Gao, Z., Li, J., 2021. Impact of high temporal resolution FY-4A Geostationary Interferometric Infrared Sounder (GIIRS) radiance measurements on Typhoon forecasts: Maria (2018) case with GRAPES global 4D-Var assimilation system. *Geophys. Res. Lett.* 48 (15) <https://doi.org/10.1029/2021GL093672>.
- Zhang, P., co-authors, 2019. Latest progress of the Chinese meteorological satellite program and core data processing technologies. *Adv. Atmos. Sci.* 36 (9), 1027–1045. <https://doi.org/10.1007/s00376-019-8215-x>.
- Zhang, Y., Zhang, F., Stensrud, D.J., 2018. Assimilating all-sky infrared radiances from GOES-16 ABI using an ensemble Kalman filter for convection-allowing severe thunderstorms prediction. *Mon. Weather Rev.* 146, 3363–3381. <https://doi.org/10.1175/MWR-D-18-0062.1>.
- Zou, X., Qin, Z., Zheng, Y., 2015. Improved tropical storm forecasts with GOES-13/15 imager radiance assimilation and asymmetric vortex initialization in HWRF. *Mon. Weather Rev.* 143, 2485–2505. <https://doi.org/10.1175/MWR-D-14-00223.1>.